MNRAS **000**, 1–17 (2018) Preprint 18 July 2019 Compiled using MNRAS LATEX style file v3.0

The LOFAR Tied-Array All-Sky Survey: Timing of the first binary pulsar discovered and 20 other pulsars

C. M. Tan,[1]★ TBD
[1] *Jodrell Bank Centre for Astrophysics, University of Manchester, Oxford Road, Manchester, M13 9PL, United Kingdom*

Accepted XXX. Received YYY; in original form ZZZ

ABSTRACT

Key words: keyword1 – keyword2 – keyword3

1 INTRODUCTION

The LOFAR Tied-Array All-Sky Survey (Coenen et al. 2014; Sanidas et al. 2019, LOTAAS;) is an all-Northern-sky survey conducted with the LOFAR telescope (van Haarlem et al. 2013) to search for pulsars and fast transients. LOTAAS is conducted at a central observing frequency of 135 MHz, with a bandwidth of 32 MHz. As of January 2019, 1913 of the 1953 planned pointings of the survey have been observed and processed, yielding a total of 73 new pulsar discoveries. Another goal of LOTAAS is to characterise the properties of all pulsars detected at very low radio frequencies around 150 MHz in the Northern sky. This meant that for new pulsar discoveries, timing observations across a large range of radio frequencies is required to model them.

The radio spectra of pulsars are typically described by a simple power law, where the flux density of a pulsar, S_ν at an observing frequency ν follows the following relationship : $S_\nu \propto \nu^\alpha$, in which α is the spectral index of the pulsar. In general, pulsars are steep spectrum radio sources, where Bates et al. (2013) found an average spectral indices of $\alpha = -1.4$, with a 1σ dispersion of 1. A later study of 441 pulsars by Jankowski et al. (2018) yielded a mean spectral index of $\alpha = -1.60$, with a standard deviation of 0.54. The spectral indices distribution found suggests that there is a population of ultra steep spectrum, low luminosity pulsars that are likely only detectable at low observing frequencies. Hence, there is the motivation to model the spectra of the LOTAAS pulsar discoveries across a large range of radio frequencies to provide a better understanding.

The frequency evolution of the pulse profiles of pulsars is believed to follow the radius-frequency-mapping model (RFM model, Ruderman & Sutherland 1975; Cordes 1978), where the width of the pulse profile of a pulsar increases with decreasing observing frequency. This is thought to be due to the emission height of a pulsar at lower frequencies are higher, with the opening angle of the radio beam being larger at larger height above the pulsar surface. Hence, we expect to detect a number of pulsars with LOTAAS that are not visible at higher radio frequencies as the wider pulses at low frequencies are more likely to cut across our line-of-sight.

A number of pulsars are found in binary system. In most cases, they are found to have smaller spin periods than isolated pulsars, which are due to accretion of matter from their companion which spun up the pulsars to periods on the order of milliseconds (Alpar et al. 1982; Bhattacharya & van den Heuvel 1991), forming the millisecond pulsars (MSPs). One variant of MSPs is the mildly recycled binary pulsars. They often have spin periods between 10 and 100 ms and are commonly accompanied by massive white dwarfs. Their longer periods are due to the companions evolved from main sequence stars before the accretion process is completed.

Previously, (Michilli et al 2019) reported the properties of 19 pulsars discovered by LOTAAS. They reported that the sample has, on average, longer spin period and smaller spin period derivative, hinting that the LOTAAS pulsar discoveries is older than the known pulsar population. They also reported that the radio spectra of these pulsars are steeper than average, linking the age of pulsars to their emission properties.

Here, we report the multi-frequency analysis of 21 pulsars discovered by LOTAAS. We modelled the rotational and spectral properties, as well as studied the frequency evolution of the pulsar emission. The sample of pulsars includes PSR J1658+3630, the first binary pulsar discovered by the survey. PSRs J0421+3256, J1638+4005, J1643+1338 and J1657+3304 were first reported by Tyul'bashev et al. (2016, 2017, 2018) and these pulsars were blindly detected by LOTAAS around the same time. As of (press time?) there are no published timing models for these pulsars. Hence, the analysis of these pulsars is presented here.

★ E-mail: chiamin.tan@postgrad.manchester.ac.uk

Table 1. The observing span and observation length of each of the 20 LOTAAS pulsars discussed in Section 3.

PSR	Span (months)	LOFAR (minutes)	Lovell (miutes)
J0100+8023	17	15	–
J0107+1322	13	15	42
J0210+5845	10	10	–
J0421+3255	21	10	–
J0454+4529	13	10	–
J1017+3011	11	10/15	–
J1624+5850	20	10	–
J1638+4005	15	10	–
J1643+1338	18	10	42/15
J1656+6203	20	10	–
J1657+3304	15	10	–
J1713+7810	18	10	–
J1741+3855	15	15/10	–
J1745+1252	16	10	–
J1749+5952	22	10	12
J1810+0705	22	10	12
J1916+3224	22	10	12
J1957−0002	20	10	–
J2036+6646	11	10	–
J2122+2426	17	10	30

2 OBSERVATIONS AND DATA RECORDING

Whenever a pulsar is confirmed by a follow-up observation with LOTAAS, the pulsar is added to the monthly LOTAAS timing campaign. The pulsars are observed with all 24 HBA stations of the LOFAR core. The lengths of individual observations of each pulsar depend on the signal-to-noise ratio (S/N) of the pulsar and are listed in Table 1. The data are recorded in dual-polarization, complex frequency channels, with 400 sub-bands of 195.3 kHz each, centred at an observing frequency of 149.8 MHz. The data are then processed with the automated Pulsar Pipeline (PulP; Stappers et al. 2011; Kondratiev et al. 2016), which coherently dedisperses the data to the DM of the pulsar and then folds at the best known spin period of the pulsar using DSPSR (van Straten & Bailes 2011). An *archive* file is produced from each observation, with 1024 phase bins and sub-integration length of 5 seconds. The observation length of each pulsar, excluding J1658+3630 is shown in Table 1.

The discoveries are also observed with the Lovell Telescope at Jodrell Bank, at a central observing frequency of 1532 MHz. Initially, each pulsar was observed for 4-5 times over a span of about 10 days. Each observation during the campaign is between 30 minutes and 1 hour long. If the pulsar is detected, a lower cadence observing campaign is continued, with each source typically observed once every fortnight, depending on the availability of the telescope. The observation length of the detected pulsars is shown in Table 1, where it depends on the S/N of the initial detection. The observations are conducted at a central observing frequency of 1532 MHz, with a bandwidth of 384 MHz across 768 channels. They are detected and processed with the digital filterbank backend (DFB), where the data are incoherently dedispersed to the DM of the pulsar and folded at the best known period. The folded *archive* files have sub-integrations that are 10 s long and 1024 phase bins.

The pulsars were also observed at a central observing frequency of 334 MHz with the Lovell Telescope for 30 minutes. The data have a bandwidth of 64 MHz across 512 frequency channels and are processed with the DFB. The folded *archive* files have sub-integrations of 10 s and 512 phase bins. Since only one observation is made for each pulsar, the data at this frequency are only used to study the profile evolution and spectral properties.

If a pulsar is not detected with the Lovell Telescope at 1532MHz, a dense observing campaign with the full LOFAR core is conducted. Four observations of 15 minutes each were conducted over a period of 10 days, with at least two of the observations over consecutive days. The data recording and processing follows the same setup used for the monthly timing campaign.

To model the binary orbit, two dense observing campaign with the LOFAR core were conducted for PSR J1658+3630 to supplement the monthly observations. In the first dense campaign, the pulsar is observed for five minutes on a weekly cadence between 2017 January 24 and 2017 April 24. Two additional sets of observations were made, with the first being sets of five observations over two hours, each five minutes long, made over five consecutive days between 2017 February 23 and 2017 February 27. The second set consists of eight five minute observations made over 12 hours on 2017 March 6. Only the Stokes I data were recorded for these observations, with a central frequency of 149.8 MHz and 6400 12.2 kHz channels. The data were incoherently dedispersed to the DM of the pulsar and folded to the best known ephemeris at the time of the observations, producing *archive* files with 10 s sub-integrations and 256 phase bins.

The interim timing solution of PSR J1658+3630 showed that the binary companion has a large minimum mass of $0.87 M_{\odot}$. Mass measurements of both the pulsar and the binary companion is possible by measuring the Shapiro delay of the pulsar signal due to its companion if the system has a low inclination angle. Hence a second dense campaign for PSR J1658+3630 is conducted which includes 24 10 minute observations made over a period of 6 months between 2017 November and 2018 May. In addition, six 1-hour observations, with gaps of 1 hour between observations were made when the predicted orbital phase of the pulsar is 0.25, which is when the binary companion is passing in front of the pulsar. Furthermore, three 2-hour observations were made when the predicted orbital phases are 0,0.5 and 0.75 respectively. These data were recorded and processed using the same method as the monthly timing observations.

PSR J1658+3630 was also observed with three of the international LOFAR stations in Germany, operated by the German LOng Wavelength consortium. A single observation between 1 and 3 hours long is made on a weekly basis between 2017 May and 2018 May and on a bi-weekly basis between 2018 June and 2018 October. A dense observing campaign was conducted on 2017 July where the pulsar was observed for 21 2-hour epochs with 2 different international LOFAR stations between 2017 July 1 and 2017 July 3. The observations were conducted at a central frequency of 153.8 MHz and a bandwidth of 71.5 MHz across 366 subbands. The data were recorded as complex frequency channels and then coherently dedispersed to the DM of the pulsar and folded using the best ephemeris of the pulsar available in

2017 July, producing *archive* files with 10 s sub-integrations and 1024 phase bins.

3 PULSAR TIMING

The folded *archive* files obtained from the observations were analysed with PSRCHIVE (Hotan et al. 2004). The pulse times-of-arrival (TOAs) of each pulsar were measured by cross-correlating the integrated pulse profiles of each observation with an analytical, noise free template. The templates were created by fitting a number of von Mises functions, depending on the complexity of the pulse profiles, with PAAS. The LOFAR observations are split into 2 frequency channels, with central frequencies of 128 MHz and 167 MHz in order to measure the DM. Different templates were made for each observing frequency, taking into account possible profile evolution. A phase-connected timing solution was then determined by modeling the TOAs with TEMPO2 (Edwards et al. 2006; Hobbs et al. 2006). Any offsets between the TOAs obtained with LOFAR and the Lovell telescope were corrected by fitting a jump between the two sets of data. The Solar System ephemeris DE405 is used to model the motion of the bodies in the Solar System in order to convert the topocentric TOAs into barycentric TOAs.

In order to phase-connect the monthly TOAs, TOAs obtained from the dense campaigns were used to refine the spin period of each pulsar. The updated spin periods were then used to model the other TOAs, subsequently fitting for the position and the spin-period derivative.

The initial observations of PSR J1658+3630 showed that the apparent spin period of the pulsar changes periodically over time, due to the motion of the pulsar in a binary orbit. We used the FITORBIT tool of PSRTIME (REF) to model the apparent changes in period, fitting for the orbital parameters of the binary system. An initial timing solution containing estimates for the binary parameters of the pulsar was produced and then used to process the subsequent observations, in order to refine the rotational and binary parameters of the pulsar. Subsequent analysis of PSR J1658+3630 will be presented in Section 6.2

The timing solutions of the 20 isolated pulsars are shown in Table 2, and the derived properties based on the rotational parameters are shown in Table 3. The timing residuals of the 20 pulsars using the best solution are shown in Figure 1. The location of the pulsars in the P-$\dot{P}$-diagram are shown in Figure 2.

The properties of most of the pulsars presented here are well modelled with just a period and period derivative, after correcting for the position, as shown by the small timing residuals obtained. However, PSRs J0210+5845 and J0421+3255 showed large timing residuals relative to the error bars of their TOAs. The timing residuals of PSR J0210+5845 suggest that the pulsar either has large timing noise related to its small characteristic age of about 200 kyr, or there are extra frequency derivatives needed to model the TOAs, which would require a longer observing span. PSR J0421+3255 has a wide pulse profile which increases the uncertainties of individual TOAs. Furthermore, two of the observations of PSR J0421+3255 have TOAs that are offset compared to the rest of the observations by roughly 20% of a pulse phase. These observations are not used to model the properties of PSR J0421+3255, as we later found that the pulses from these observations coincide with a change in the integrated pulse profile (See Section 4 for further discussion).

The initial timing observations suggest that PSR J1643+1338 is a low S/N pulsar. However, after 10 months of observations, the timing position of the pulsar was found to be different from the observing position by 13 arcmin. The new position was used from 2018 May, with the pulsar detected at a S/N about 6 times higher than before. Although the position offset of the pulsar is roughly 4 times the full-width half-maximum (FWHM) of the LOFAR core beam at 149 MHz of 3.5 arcmin, the relatively large S/N of the pulsar allowed us to detect it in a side lobe of the beam.

The TOA uncertainty of individual observations of PSR J1657+3304 varied by about a factor of 20 across the observation span. This corresponds to a large variation in the observed flux density in the pulsar, with S/N changes of a factor of 10. Further analysis and discussion on PSR J1657+3304 are presented in Section 6.1.

The 20 LOTAAS discoveries discussed in this section are indicated as small red crosses in Figure 2. Most of the pulsars studied here are located in the lower right of the P-$\dot{P}$-diagram, where the characteristic ages are $\gtrsim$ 10 Myr. This suggests that the population that is probed here is older than the general pulsar population. However, this sample only represents a fraction of all the pulsars discovered by LOTAAS. A more general study on the properties of all LOTAAS discoveries will be conducted after the conclusion of the survey. A notable exception to this sample is PSR J0210+5845. It is located in a more sparsely populated region of the diagram, with a characteristic age of 200 kyr and surface dipole magnetic field of 1.1×10^{13} G. The pulsar also shows large timing residuals, which could be timing noise related to its small characteristic age. Additionally, the rotational properties of the pulsar provide a possibility to measure the second derivative. However, a longer observation span of at least a few years is required to distinguish it from timing noise. It is also the slowest-spinning pulsar among the sample of pulsars studied here.

4 PULSE PROFILES

The pulse profiles of the pulsars at 149 and 1532 MHz were obtained by adding the integrated pulse profiles obtained from each observation together with PSRADD, after aligning the profiles from different observations using the timing solutions obtained in Table 2. We measured the pulse widths and the duty cycles of the pulsars at 10% and 50% of the maximum using the following method. First, noise free templates of the pulse profiles were generated by fitting von Mises functions using PAAS. The observed off-pulse region was then used to generate a noise distribution. One thousand simulated pulses were generated by creating new noisy profiles combining the noise free template with the simulated noise. These were then fitted with the noise free template allowing height, width and position to vary. The widths of the resultant von Mises profiles from the 1000 trials were then used to determine the mean width and error. The results are presented in Table 4.

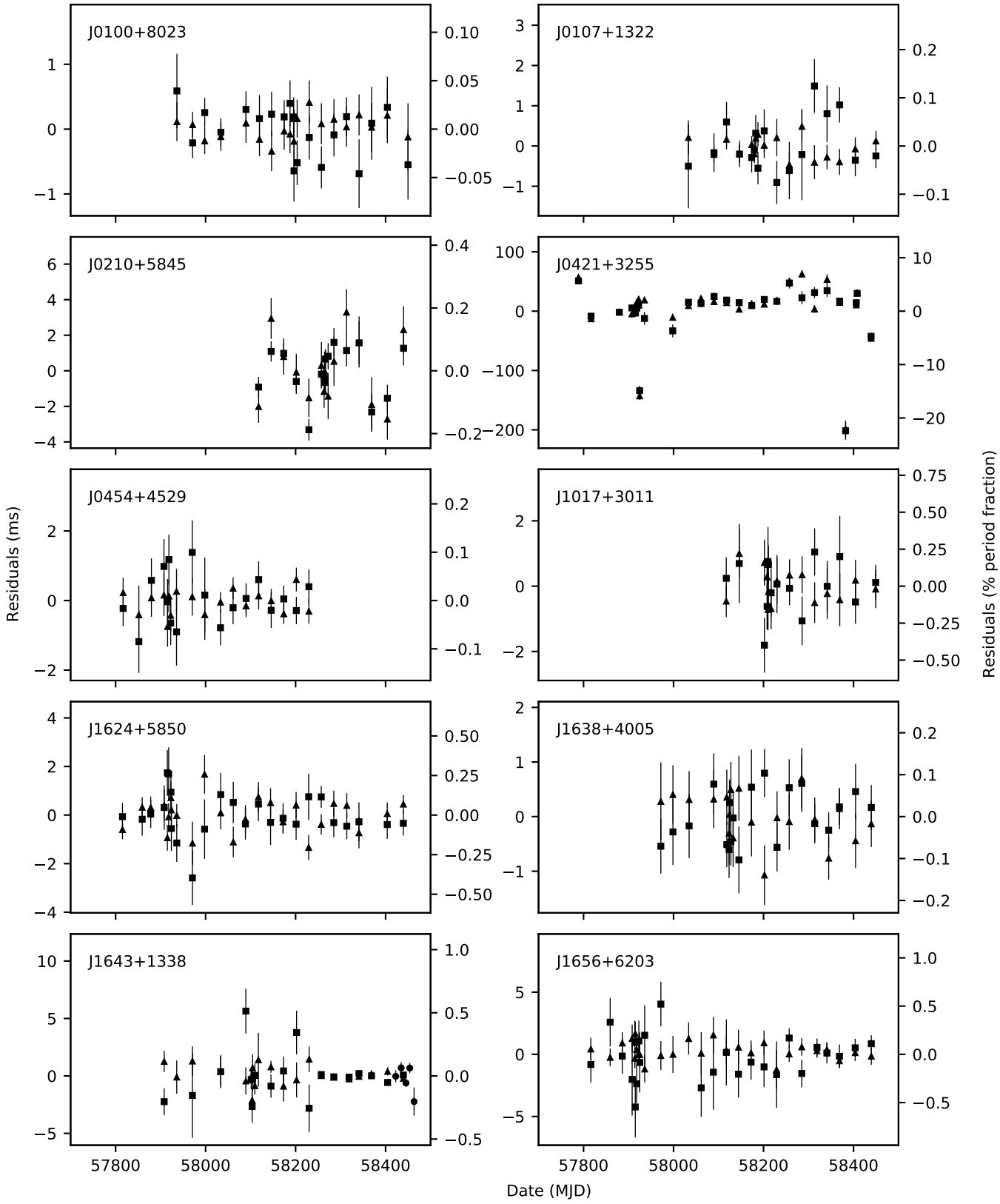

Figure 1. The residuals from the timing model of the TOAs from the 20 pulsars presented in Table 2. The different symbols represents the different observing frequencies, with triangles for the lower part of the LOFAR band (128 MHz), squares for the upper part of the LOFAR band (167 MHz) and dots for the Lovell telescope at 1532 MHz.

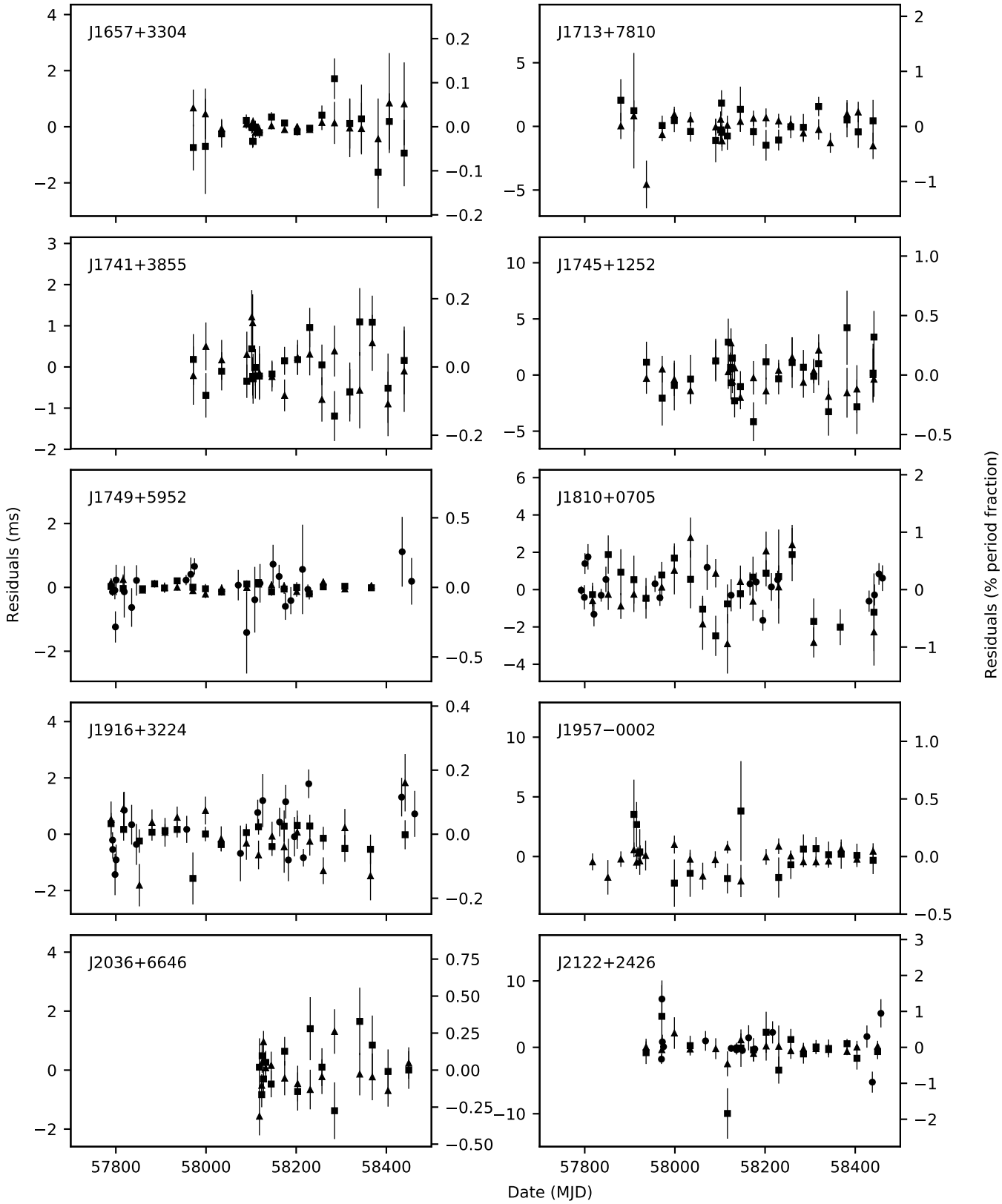

Figure 1. Continued.

Table 2. The timing solutions of 20 pulsars, showing the positions, reference epoch, spin period, spin-period derivative, DM, number of TOAs used to model the pulsars and the timing residuals after modelling the pulsars.

PSR (J2000)	RA (J2000)	DEC (J2000)	Epoch (MJD)	P (s)	$\dot{P}$ (10^{-15})	DM ($pc\,cm^{-3}$)	N_{TOA}	TRES µs
J0100+8023	01:00:16.09(1)	+80:23:41.75(3)	56676	1.4936009186(2)	0.3543(6)	56.0062(8)	40	242
J0107+1322	01:07:39.95(2)	+13:22:31.7(8)	57972	1.1973833938(1)	0.687(3)	21.671(1)	34	331
J0210+5845	02:10:55.4(1)	+58:45:04(1)	58011	1.766208099(2)	134.02(2)	76.772(6)	32	1440
J0421+3255	04:21:33.2(2)	+32:55:50(10)	57310	0.900105016(1)	0.06(2)	77.02(6)	50	20744
J0454+4529	04:54:59.310(8)	+45:29:46.7(1)	56909	1.3891369360(4)	4.888(2)	20.834(2)	36	408
J1017+3011	10:17:36.29(3)	+30:11:46.1(4)	57986	0.4527850730(2)	0.57(3)	27.150(2)	30	561
J1624+5850	16:24:00.964(9)	+58:50:15.77(6)	57718	0.65180081878(2)	0.331(1)	26.403(2)	50	617
J1638+4005	16:38:16.243(6)	+40:05:56.37(6)	57491	0.76772039193(9)	0.183(2)	33.417(1)	40	435
J1643+1338	16:43:54.140(5)	+13:38:43.9(1)	57820	1.09904716266(7)	0.778(2)	35.821(1)	45	379
J1656+6203	16:56:10.29(1)	+62:03:50.41(9)	57652	0.77615531125(4)	0.844(2)	35.262(3)	52	828
J1657+3304	16:57:50.682(6)	+33:04:33.65(5)	57927	1.5702755247(1)	1.734(2)	23.9746(6)	40	191
J1713+7810	17:13:27.07(3)	+78:10:33.99(8)	57773	0.43252593524(3)	0.114(5)	36.977(3)	42	810
J1741+3855	17:41:12.341(8)	+38:55:09.90(6)	57927	0.82886088996(6)	0.206(4)	47.224(2)	40	495
J1745+1252	17:45:44.19(2)	+12:52:38.3(2)	57883	1.0598487584(1)	0.563(4)	66.141(5)	46	1434
J1749+5952	17:49:33.228(2)	+59:52:36.13(1)	57751	0.436040950719(2)	0.1519(4)	45.0694(4)	58	134
J1810+0705	18:10:47.038(7)	+07:05:36.3(2)	57770	0.30768283388(1)	0.242(4)	79.425(5)	59	1045
J1916+3224	19:16:03.468(4)	+32:24:39.70(6)	57638	1.13744972551(3)	3.4696(6)	84.105(2)	56	565
J1957−0002	19:57:42.620(7)	−00:02:06.8(2)	57674	0.96509596606(4)	0.805(1)	38.443(4)	39	621
J2036+6646	20:36:52.32(5)	+66:46:20.7(3)	57974	0.5019271782(2)	0.94(4)	50.763(2)	30	607
J2122+2426	21:22:39.02(1)	+24:26:44.9(2)	57922	0.54142115903(4)	0.127(6)	8.500(5)	47	1029

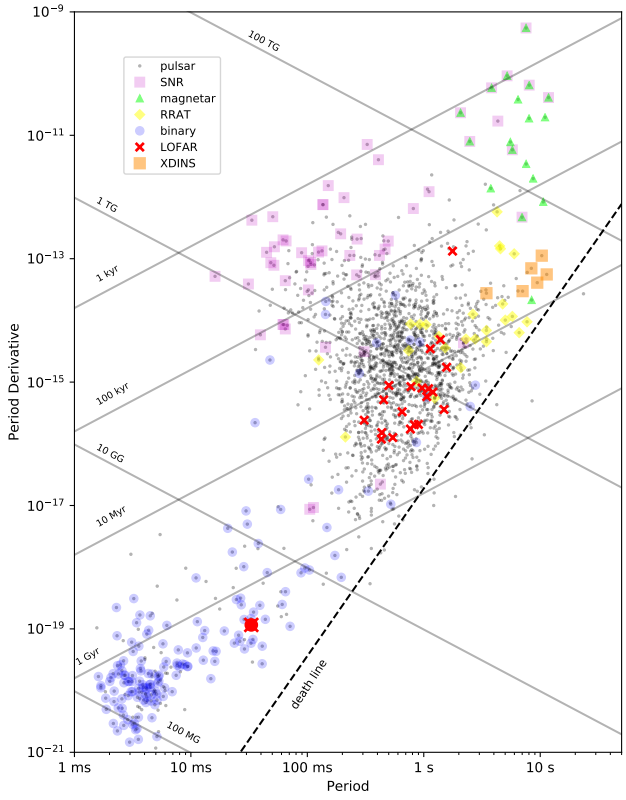

Figure 2. The *P*-$\dot{P}$-diagram of pulsars, overlaid with the 21 LOTAAS discoveries discussed here. The LOTAAS discoveries are indicated with a red cross, with PSR J1658+3630 indicated with a larger red cross with a circle in the middle. The death line plotted here is the one modelled by Equation 9 of Chen & Ruderman (1993).

Table 3. The derived properties of the 20 pulsars based on the rotational parameters obtained, showing the characteristic age, surface magnetic field strength and the rotational energy loss. The derived quantities assume that the pulsars have a dipolar magnetic field structure.

PSR	$\log t_c$ (yr)	$\log B$ (G)	$\log \dot{E}$ ($erg\,s^{-1}$)
J0100+8023	7.8	11.9	30.6
J0107+1322	7.4	12.0	31.2
J0210+5845	5.3	13.2	33.0
J0421+3255	8.3	11.4	30.5
J0454+4529	6.7	12.4	31.9
J1017+3011	7.1	11.7	32.4
J1624+5850	7.5	11.7	31.7
J1638+4005	7.8	11.6	31.2
J1643+1338	7.4	12.0	31.4
J1656+6203	7.2	11.9	31.9
J1657+3304	7.2	12.2	31.2
J1713+7810	7.8	11.4	31.7
J1741+3855	7.8	11.6	31.2
J1745+1252	7.5	11.9	31.3
J1749+5952	7.7	11.4	31.9
J1810+0705	7.3	11.4	32.5
J1916+3224	6.7	12.3	32.0
J1957−0002	7.3	12.0	31.5
J2036+6646	6.9	11.8	32.5
J2122+2426	7.8	11.4	31.5

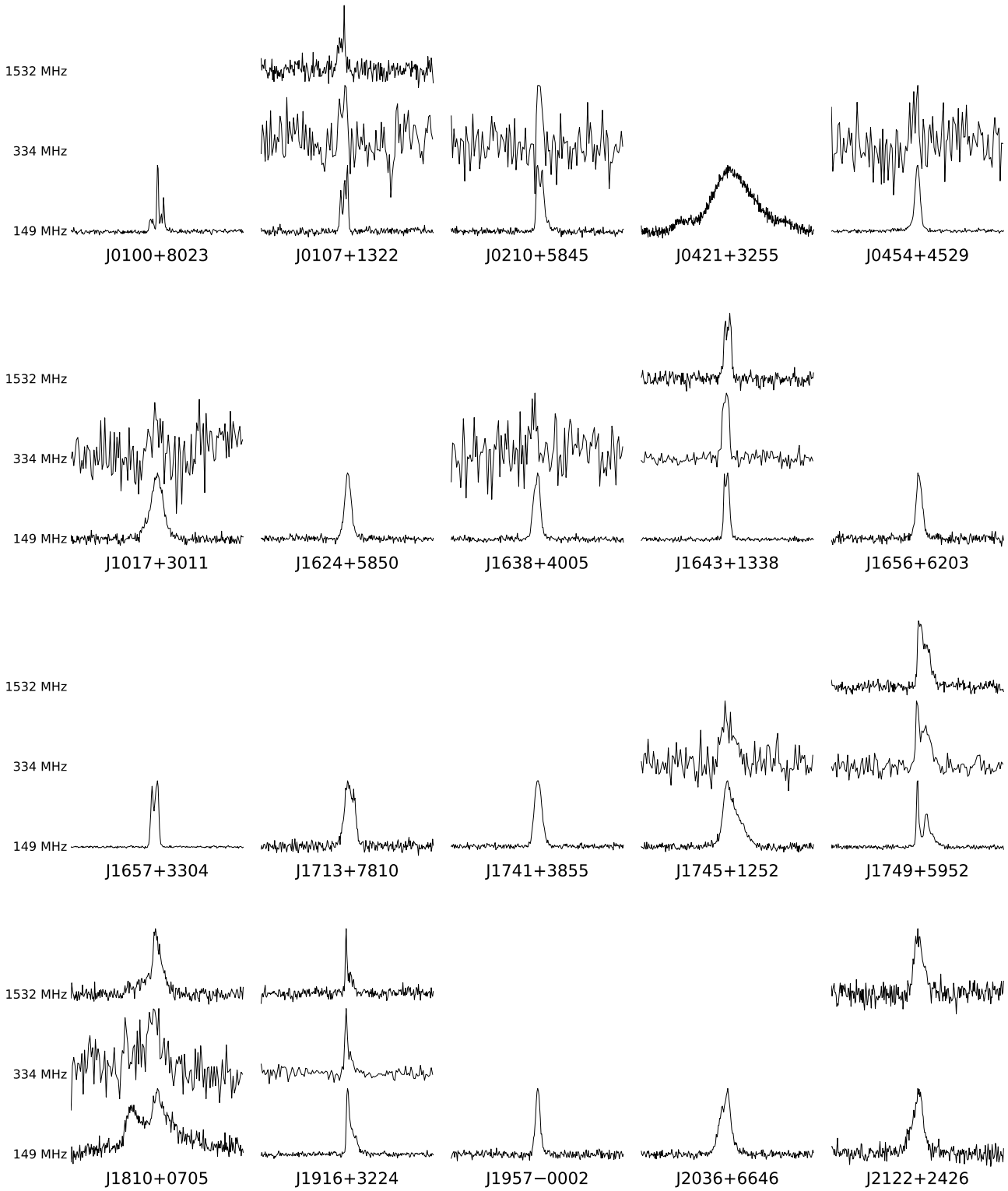

Figure 3. The pulse profiles at 149, 334 and 1532 MHz of the 20 pulsars shown in Table 2. All the profiles show 50 per cent of the pulse phase, centred around the maximum for clearer illustration, except for PSR J0421+3255, which shows the profile across the full pulse phase.

Table 4. The pulse widths and duty cycles of the pulsars shown in Fig 3.

PSR	W_{10} (ms)			δ_{10} (%)			W_{50} (ms)			δ_{50} (%)		
	149 MHz	334 MHz	1532 MHz	149 MHz	334 MHz	1532 MHz	149 MHz	334 MHz	1532 MHz	149 MHz	334 MHz	1532 MHz
J0100+8023	67(3)	–	–	4.5(2)	–	–	8.01(1)[a]	–	–	0.5361(9)[a]	–	–
J0107+1322	35.7(2)	44(2)	39(4)	2.98(2)	3.7(1)	3.2(3)	28.0(3)	32(2)	3.7(2)[b]	2.34(3)	2.7(2)	0.31(2)[b]
J0210+5845	76(3)	49(6)	–	4.3(2)	2.8(2)	–	40.9(6)	27(3)	–	2.31(3)	1.5(2)	–
J0421+3256	634(9)	–	–	70(1)	–	–	231(2)	–	–	25.6(2)	–	–
J0454+4529	48.3(8)	67(3)	–	3.48(5)	4.8(2)	–	23.54(9)	37(3)	–	1.695(7)	2.6(2)	–
J1017+3011	38.8(6)	30.3(9)	–	8.6(1)	6.7(2)	–	18.9(2)	16.6(9)	–	4.17(5)	3.7(2)	–
J1624+5850	27.0(3)	–	–	4.14(5)	–	–	14.8(3)	–	–	2.27(5)	–	–
J1638+4005	29.7(2)	33(2)	–	3.87(2)	4.3(2)	–	18.5(2)	18(2)	–	2.41(3)	2.4(2)	–
J1643+1338	31.0(1)	33.6(5)	35.9(3)	2.823(9)	3.06(5)	3.27(3)	20.8(1)	23.4(6)	25.8(4)	1.89(1)	2.13(6)	2.34(4)
J1656+6203	30.4(4)	–	–	3.91(5)	–	–	16.7(4)	–	–	2.15(5)	–	–
J1657+3304	49.8(1)	–	–	3.171(7)	–	–	38.1(1)	–	–	2.426(8)	–	–
J1713+7810	24(1)	–	–	5.6(3)	–	–	16(1)	–	–	3.7(2)	–	–
J1741+3855	38.7(4)	–	–	4.67(5)	–	–	21.2(4)	–	–	2.55(5)	–	–
J1745+1252	105.4(6)	85(4)	–	9.95(6)	8.0(4)	–	47(2)	48(6)	–	4.4(1)	4.6(6)	–
J1749+5952	26.1(3)	26.6(5)	25.1(2)	5.99(6)	6.1(1)	5.75(5)	13.3(2)[c]	14.5(11)[d]	14.7(4)	3.04(4)[c]	3.3(3)[d]	3.38(9)
J1810+0705	127(12)	46(6)	36(1)	41(4)	15(2)	11.6(4)	42.3(14)	20(5)	9.4(2)	13.8(4)	6.4(16)	3.05(5)
J1916+3224	46.6(4)	37(2)	40(2)	4.10(3)	3.2(2)	3.5(1)	11.2(1)	7.9(3)	5.2(1)	0.99(1)	0.69(2)	0.461(8)
J1957−0002	28.4(5)	–	–	2.95(5)	–	–	15.6(5)	–	–	1.62(5)	–	–
J2036+6646	31.8(2)	–	–	6.33(4)	–	–	19.5(3)	–	–	3.88(6)	–	–
J2122+2426	41(1)	–	35(1)	7.7(2)	–	6.5(2)	19.5(7)	–	15.5(8)	3.6(1)	–	2.9(1)

[a] Also measured as 30.4(3) ms and 2.04(2), see text for details.
[b] Also measured as 3.04(1) ms and 0.697(3)
[c] Also measured as 18(2) ms and 1.5(2)
[d] Also measured as 4.3(1) ms and 0.98(2)

Amongst the 20 pulsars studied here, 9 of them are only detected with LOFAR at 149 MHz. Six of these, PSRs J1624+5850, J1656+6203, J1713+7810, J1741+3855, J1957−0002 and J2036+6646, showed single peaks in their integrated pulse profiles, four of which were well modelled with just a single von Mises component. The profiles of PSRs J1713+7810 and J2036+6646 are more complex and required two components to model. The profile of PSR J1657+3304 shows two distinct peaks, both of which are well modelled with just a single component. The profile of PSR J0100+8023 is the most complex of all the pulsars studied here. It consists of four separate peaks. Two separate values of W_{50} were measured for PSR J0100+8023: 8.01 ms, which corresponds to the width of the main peak, and 30.4 ms, which is the combined width of the main peak and the fourth peak at the trailing edge of the profile, as the relative intensity of this peak is about half of the main peak.

The profile of PSR J0421+3255 showed a main peak with intensity that is much larger than two smaller peaks at either side of it. The location of the leading component of PSR J0421+3255 coincides with the position of the pulse of the two observations that have phase offset, shown in Figure 4. As the pulse profile is formed without adding the observations with phase offset, this suggests that the pulsar might undergo mode changing where there are only emission from the leading peak, which has larger intensity compared to the regular mode on these observations. Alternately, the profile change could be similar to the flaring phenomenon seen in PSR B0919+06 (Perera et al. 2015), where the emission of the pulsar appears to shift earlier in pulse phase compared to the regular emission. However, the flares seen in PSR B0919+06 last on the order of seconds while in PSR J0421+3255, they last more than a single 15 minutes observation.

Five of the pulsars are detected with both LOFAR at 149 MHz and the Lovell telescope at 334 MHz. PSRs, J0454+4529, J1017+3011, J1638+4005 and J1745+1252, shows complex single peaked profiles that are modelled with multiple components at 149 MHz. The detections at 334 MHz for PSRs, J0454+4529, J1017+3011 and J1638+4005 are too weak for the profiles to be well modelled. However, the general shape of the profiles are similar to those at 149 MHz.

The profiles of PSRs J0210+5845 and J1745+1252 shows signs of a possible scattering tail. We measured the scattering index, α_s and timescale, τ_s of these pulsars across the LOFAR band using the method described in Geyer & Karastergiou (2016), assuming an isotropic scattering screen. The LOFAR band is split into 8 sub-bands and the scattering time in each band is measured, with α_s fitted assuming a power law relationship between scattering time and frequency. The measured α_s and τ_s at 1000 MHz of PSR J0210+5845 are -2.4 ± 0.5 and 0.2 ± 0.2 ms respectively, while the measured α_s and τ_s at 1000 MHz of PSR J1745+1252 are -1.0 ± 0.1 and 5 ± 1 ms respectively. The measured scattering indices of the two pulsars are much lower than the theoretically predicted relationship of $\tau_s = -4$ or -4.4. However, this was seen on other pulsars observed with LOFAR (Geyer et al. 2017).

PSR J2122+2426 is detected with LOFAR at 149 MHz and the Lovell telescope at 1532 MHz. The pulsar shows single-peaked profiles that are modelled with 2 components at both frequencies. However, the positions of the second component are different at the two observing frequencies, where it appears before the main component at 149 MHz but after the main component at 1532 MHz. This evolution is similar to what is observed with PSR B0809+74 by Hassall et al. (2012). However, the observation of the pulsar at 334 MHz is strongly affected by RFI and so we cannot be sure if this is the same behaviour.

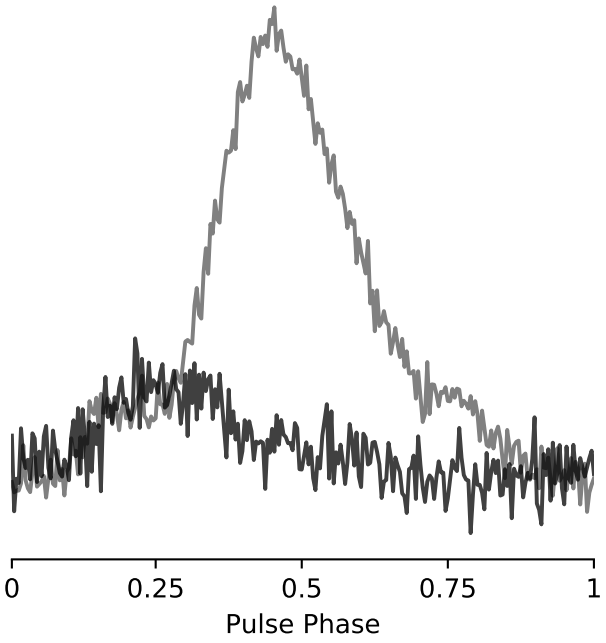

Figure 4. The integrated pulse profile of PSR J0421+3255 across all observations expect the two with phase offset (*grey*), seen in the timing residuals in Figure 1, overlaid with the integrated pulse profile summed over the two observations with phase offset compared to the rest of the observations (*black*). The phase of the pulses in the observations where the offset occurred coincides with the leading peak of the integrated pulse profile.

The other 5 pulsars, PSRs J0107+1322, J1643+1338, J1749+5952, J1810+0705 and J1916+3224 are detected with LOFAR and the Lovell telescope at both 334 and 1532 MHz. These detections allowed us to study the evolution of the pulse profiles across multiple different observing frequencies. Here we describe the frequency evolution of these pulsars one by one.

PSR J0107+1322

PSR J0107+1322 shows three distinct peaks in its profile at 149 MHz, which are well modelled with three components that increase in intensity from the leading to the trailing peaks. However, the profiles at 334 and 1532 MHz only show two distinct peaks; a weak leading peak and a strong trailing peak. The profiles are better modelled with two components rather than with three components. While the W_{10} of the pulsar suggests that the pulse width increases from 149 MHz to 334 MHz, contrary to the RFM model. We suspect this

Table 5. The separation between the 2 major components in PSRs J1643+1338, J1749+5952 and J1916+3224 at 149, 334 and 1532 MHz in ms.

Pulsar PSR	Frequency MHz	Separation between components ms
J1643+1338	149	10.1(1)
	334	12.6(5)
	1532	14.5(3)
J1749+5952	149	11.35(8)
	334	10.0(5)
	1532	8.4(2)
J1916+3224	149	15.6(5)
	334	12(2)
	1532	10.9(12)

could be just due to how the leading peak of the profile at higher frequencies is modelled – as a single, broader component rather than with two more narrow components in the case of the profile at 149 MHz. Higher S/N is required for the observations of PSR J0107+1322 at higher frequencies to better model the leading peak, which might manifest itself as two separate peaks.

PSR J1643+1338

PSR J1643+1338 shows two distinct peaks in its profiles at all three observing frequencies, all of which are well modelled with just a single component per peak. However, both W_{10} and W_{50} of the pulsar are shown to increase with increasing frequency, suggesting that the components widen with increasing frequency, contrary to the RFM model. We also measured the separation between two components (Table 5). We found that the separation between the components increases at higher frequencies as well, further evidence that the pulsar does not conform to the RFM model. While the behaviour of PSR J1643+1338 is unusual, the anti-RFM profile evolution has been seen in several other pulsars before by Hassall et al. (2012) and Pilia et al. (2016).

PSR J1749+5952

The pulse profiles of PSR J1749+5952 show two distinct peaks at 149 and 334 MHz, while at 1532 MHz, the trailing peak seems to merge with the leading peak. The profiles at 334 and 1532 MHz can be modelled relatively well with just 2 components. However, the profile at 149 MHz requires three components; the two main components describing each peak and a bridge component that is fitted across the profile. The W_{50} values of the profiles at 149 and 334 MHz both show two distinct distribution of measurements. We found that this is due to the trailing peak of both profiles having roughly half the intensity of the leading peak. The smaller values in Table 4 correspond to the width of the main peak at half maximum while the larger values correspond to the width of the whole profile.

The values of W_{50} that correspond to the width of the main peak suggest that the width of the main peak increases with increasing frequency. This is inconsistent with RFM where we expect individual components to widen at lower frequencies. However, measurements of the separation of the components corresponding to the two peaks seen in the profile, shown in Table 5 suggest that the separation between components decreases with increasing frequency, which is in agreement with RFM.

PSR J1810+0705

The integrated pulse profiles of PSR J1810+0705 show significant frequency evolution. At 149 MHz, the profile shows 2 distinct peaks of about equal intensity and at 1532 MHz, the intensity of the leading peak relative to the trailing peak is reduced. The pulsar shows 2 distinct peaks at 334 MHz as well, however, the low S/N of the observation does not allow us to get a good estimate of the relative intensity between the peaks. The W_{10} of the pulsar also shows a large decrease with increasing frequency, suggesting that the separation between the two components decreases with increasing frequency as expected. Due to the complex structure of the profile of PSR J1810+0705 at 149 MHz, we are unable to model the two peaks as distinct components to measure the component separation. The templates that were used for pulsar timing requires several components for each peak to produce an adequate model of the pulse profiles.

PSR J1916+3224

PSR J1916+3224 shows a strong main peak and a trailing, wider component at all 3 observing frequencies. The evolution of the pulse profile is found to follow the RFM model, where the W_{50} of the profiles, which correspond to the width of the main peaks, decreases as observing frequency increases. While the measured W_{10} suggests the profile width is constant between 334 and 1532 MHz, the separation between the two main components (Table 5) decreases with increasing observing frequency, in agreement with RFM model.

5 FLUX DENSITIES AND SPECTRAL INDICES MEASUREMENTS

The LOFAR observations are flux-calibrated using the method described in Kondratiev et al. (2016). The calibrated data of individual observations are then split into 2 frequency bands to measure the flux densities of the pulsars at 128 and 167 MHz respectively. The average flux density of each pulsar is then computed from these observations. We found that the initial pointing position of the observations of most of the pulsars are offset from the measured position obtained through pulsar timing by an order of an arcminute. The pointing offset was corrected for several of the pulsars studied here in later observations. We attempted to correct the measured flux densities due to loss in sensitivity as a result from the offsets from the early observations. However, we found that pulsars with initial pointing positions that are offset from the timing position by less than 1 arcmin did not show any improvement in S/N after updating the pointing position, while those with offset of more than 1 arcmin showed S/N improvement that is less than expected. Hence, we decided that, for pulsars with an initial pointing offset less than 1 arcmin, flux density measurements for all observations are used without applying any correction,

while for those with larger offsets, only the observations after the pointing position is corrected are used to measure the flux density of the pulsars. The error in the measured flux densities of each frequency band of a single observation is conservatively estimated to be 50 per cent (Bilous et al. 2016).

The flux densities of pulsars detected at 334 and 1532 MHz are estimated using the radiometer equation (Lorimer & Kramer 2005). The receiver temperature T_{rec} of the 334 MHz receiver is 50 K and the sky temperature T_{sky} in the direction to the relevant pulsar is estimated by extrapolating the T_{sky} at 408 MHz (Haslam et al. 1982) with a spectral index of −2.55 (Lawson et al. 1987; Reich & Reich 1988). The Gain G of the receiver is 1 K Jy^{-1} and the bandwidth is 64 MHz. As for the 1532 MHz observations, T_{rec} = 25 K, G= 1 K Jy^{-1} and the bandwidth is 384 MHz. We estimated the average RFI fraction of each observation at 1532 MHz to be 20 per cent of the bandwidth and 5 per cent of the observing length, while at 334 MHz, the fraction is 20 per cent of the bandwidth and 20 per cent of the observing length. Upper limits for the non-detections are estimated with the radiometer equation with a threshold S/N of 10 and estimated pulse width based on the measured W_{50} at 149 MHz. The uncertainty on the flux density of a single observation is estimated to be 20 per cent.

The flux densities and the measured spectral indices are shown in Table 6. Only pulsars detected by LOFAR and another observing frequency have a measured spectral index. An upper limit in spectral index is placed for pulsars with measured flux densities only in the LOFAR band. The spectral indices of the pulsars are modelled using a single power law where $S_\nu \propto \nu^\alpha$, where S is the flux density, ν is the observing frequency and α is the spectral index of the pulsar. The measured spectral indices of the pulsars are also shown in Table 6.

We then compute the average spectral index of the 19 pulsars, while using the upper limits as the measured spectral index whenever it is relevant. We found that the average spectral index of the 19 LOTAAS discoveries studied here to be $\alpha = -1.9 \pm 0.5$, lower than the average found by Bates et al. (2013) and Jankowski et al. (2018) of $\alpha = -1.4$ and $\alpha = -1.6$ respectively. This suggests that the discoveries we made have steeper spectra than the average pulsars and they will be less likely to be detected by surveys at higher frequencies.

However, the spectra of several of the pulsars are not well-modelled with a single power law. Figure 5 shows the spectral fit of PSRs J0210+5845, J1745+1252 and J1916+3224 with a single power law. The flux densities of PSR J0210+5845 suggest that the spectrum is less steep at 128 and 167 MHz and steeper at higher frequencies, indicating that the spectrum could be a broken power law with two different spectral indices below and above 200 MHz, or that there is a spectral turnover at the LOFAR observing frequencies of about 150 MHz. The spectrum of PSR J1745+1252 is well fitted with a single power law between 128 and 334 MHz. However, the upper limit in flux density at 1532 MHz suggests that the spectrum becomes steeper at high observing frequencies. The spectrum of PSR J1916+3224 suggests that the flux density at 334 MHz is too large and too small at 1532 MHz when fitted with a single power law. The actual spectrum of the pulsar could be similar to PSR J0210+5845 where a broken power law is required.

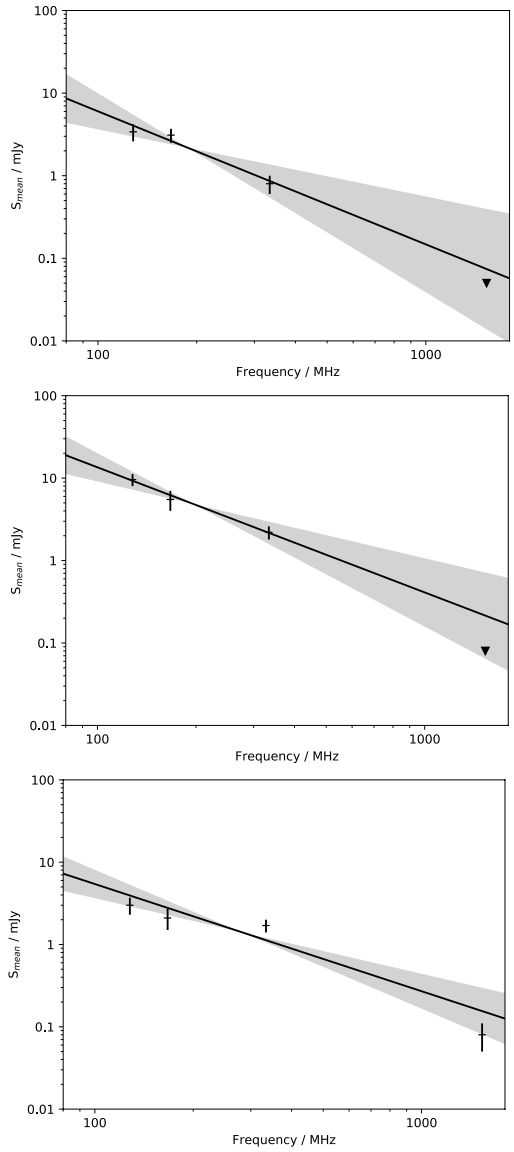

Figure 5. The spectra of PSRs J0210+5845 (*top*), J1745+1252 (*centre*) and J1916+3224 (*bottom.*), fitted with a simple power law. The fitted spectral indices are shown as black lines, with a 1σ uncertainty region shaded in grey. The triangles denote the upper limit in flux densities of the non-detections at the relevant observing frequencies. The fitted spectral indices and uncertainties of these pulsars can be found in Table 6.

The fraction of pulsars that were not well-fitted with a single power law is in line with what is found by Bilous et al. (2016) and Jankowski et al. (2018). In those cases, the pulsars are either fitted with a broken power law spectra or a log-parabolic spectra with a turnover frequency. The three pulsars discussed are unlikely to be part of the Gigahertz-peaked spectra pulsars (Kijak et al. 2011; Rajwade et al. 2016), as the flux densities measured at 334 MHz are lower than the flux densities at LOFAR frequencies. The Gigahertz-peaked spectra pulsars are expected to have turnover frequencies of between 0.6-2 GHz. In order to better study the spectra of these sources and other LOTAAS discoveries, we would require observations conducted at frequencies not covered by this work.

Table 6. Flux densities measurements of each pulsar.

PSR	128 MHz	167 MHz	334 MHz	1532 MHz	α
J0100+8023	2.4(7)	1.5(4)	<0.3	<0.03	< −2.2
J0107+1322	2.8(10)	1.8(7)	0.46(9)	0.07(3)	−1.5(5)
J0210+5845[a]	3.4(8)	3.1(6)	0.8(2)	<0.05	−1.6(8)
J0421+3255	27(6)	16(4)	<2.0	<0.16	< −2.8
J0454+4529[a]	7(17)	2.7(7)	0.44(9)	<0.04	−2.8(7)
J1017+3011[a]	3.4(5)	1.9(4)	0.31(6)	<0.06	−2.5(6)
J1624+5850	2.5(5)	1.3(3)	<0.4	<0.04	< −1.9
J1638+4005	3.1(5)	1.7(3)	0.34(7)	<0.06	−2.3(6)
J1643+1338	11(4)	9(3)	2.6(5)	0.11(3)	−1.9(4)
J1656+6203	2.6(5)	1.2(3)	<0.5	<0.04	< −1.6
J1657+3304[b]	–	–	–	–	–
J1713+7810	1.7(6)	0.9(3)	<0.6	<0.07	< −1.2
J1741+3855	3.1(7)	2.0(5)	<0.5	<0.06	< −1.9
J1745+1252	9.6(16)	5.5(15)	2.2(4)	<0.08	−1.5(6)
J1749+5952	5.9(21)	4.1(14)	2.3(5)	0.16(7)	−1.4(5)
J1810+0705	14(4)	11(3)	2.6(5)	0.22(6)	−1.7(3)
J1916+3224	3.0(7)	2.1(6)	1.7(3)	0.08(3)	−1.3(4)
J1957−0002	7.5(15)	3.5(7)	<0.5	<0.03	< −2.8
J2034+6646[a]	5.0(10)	2.1(6)	...[c]	<0.06	< −1.7
J2122+2426	4.0(12)	2.0(9)	...[c]	0.07(2)	< −1.6

[a] These pulsars have no observations that were pointed towards their timing positions.
[b] PSR J1657+3304 showed large flux density variation across the observing span with LOFAR. A discussion about it will be presented in Section 6.1
[c] The observations are strongly affected by RFI. Hence, we were not able to obtain a reliable flux density estimates from them.

6 NOTABLE PULSARS

6.1 PSR J1657+3304

The emission of PSR J1657+3304 shows several interesting properties. Firstly, it shows long-term flux density variation over the observation span. We measured its flux densityat 149 MHz across 15 observations over 347 days, shown in Table 7, and it varies by a factor of 10 over approximately 300 days before staying constant at low flux density (1.5 mJy) after MJD 58300. The magnitude of the variation is much larger than any other pulsars discussed in this work. The variation is unlikely to be due to interstellar scintillation as the expected scintillation bandwidth at 149 MHz is only about 2 MHz according to the NE2001 model (Cordes & Lazio 2002), much smaller than the bandwidth of the LOFAR timing observations of 78 MHz. We attempted to identify any period derivative changes that correlates with the flux density variation, as the changes in flux density of the pulsar could be due to long-term mode changing that is often accompanied with changes in the period derivative of the pulsar (Kramer et al. 2006; Lyne et al. 2010). Unfortunately, we did not detect any noticeable change in period derivative.

Single observations of the pulsar also showed nulling over durations between several pulses to a few minutes (Fig. 6). We estimated the nulling fraction of each observation of PSR J1657+3304 following the method of Wang et al. (2007), where the pulse energy distribution of the pulsar is compared with the off-pulse energy distribution. We also tested whether the nulling fraction obtained are the same for both high and low flux density observations, by increasing the noise level of the high flux density observations to have the same S/N as the low flux density observations and then calculating the nulling fraction. We find that the measured nulling fraction changes with S/N as it is more difficult to separate the pulses from the nulls. Hence we only estimated the nulling fraction from the 4 observations with flux densities above 10 mJy. The average nulling fraction is found to be 34 per cent.

Table 7. The flux density and the estimated nulling fraction of individual observations of PSR J1657+3304.

Observation date MJD	Flux Density mJy	Nulling Fraction
58034	3.6	–
58089	9.4	–
58101	6.5	–
58103	6.3	–
58104	7.2	–
58118	9.4	–
58145	11.0	0.44
58174	15.8	0.29
58202	17.2	0.31
58230	15.4	0.33
58257	4.9	–
58284	2.2	–
58318	1.5	–
58344	1.6	–
58381	1.4	–

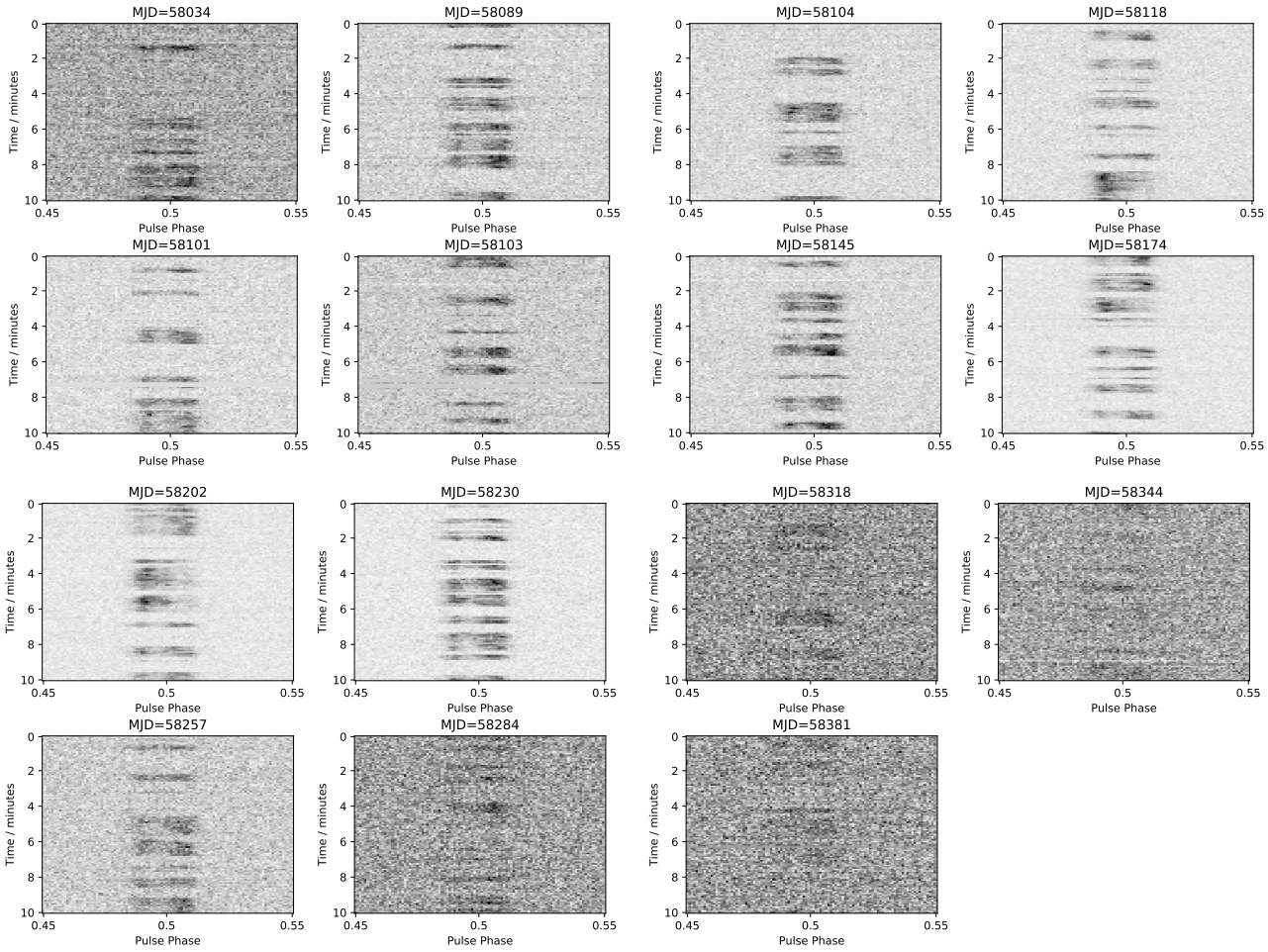

Figure 6. The sub-integration against pulse phase plots of all 15 different observations of PSR J1657+3304 presented in Table 7. Each sub-integration is 5 s long, corresponding to between 3-4 pulses of the pulsar. There is a trend of increasing flux density of the pulsar from MJD 58034 to about MJD 58100 and decreasing flux density from MJD 58230 to MJD 58284. The nulling of the pulsar can also be seen in most of the observations; the shortest null is about 5 s as seen in the observation taken on MJD 58230 and the longest null seen in these observations is about 4 minutes from the observations taken on MJD 58034 and MJD 58284. The observation taken at MJD 58202 shows clear mode changing between the on-phase at 0-2 minutes and at 3-6 minutes, where the profile switches from a double peaked structure to a single peak structure. The plots are zoomed into 10% of the pulse phase of the pulsar.

In addition to nulling, we observed short-term mode changing in some observations, where the pulse profile switches between the commonly occurring double-peaked structure to only the leading peak being present (Fig. 7). While most of the mode changing happens between nulls, there is an instance of mode changing in MJD 58118 that does not involve a period of nulling. The duration of the occurrence of each instance of the less common mode is between 1-5 minutes, similar to the duration of the nulls.

PSR J1657+3304 was observed with the Lovell Telescope at both 334 and 1532 MHz. The observation at 334 MHz is strongly affected by RFI, and the pulsar is not detected in 4 30-minute observations at 1532 MHz. However, the observations at 1532 MHz coincide with the period when PSR J1657+3304 showed low flux density at LOFAR observing frequencies. This gives an upper limit to the flux density of the pulsar at 1532 MHz of 0.06 mJy when it is in the low flux density state. Further observations are planned when the flux density of the pulsar at LOFAR observing frequencies increases.

6.2 PSR J1658+3630

The low eccntricity of the orbit of PSR J1658+3630 meant we used the ELL1 binary model (Lange et al. 2001) to model the TOAs. The timing model is shown in Table 8 and the timing residuals as a function of both time and binary phase are shown in Fig. 8. The pulsar has a spin period of 33.0 ms and spin period derivative of 1.16×10^{-19} s s^{-1}, placing it in the location of the P-$\dot{P}$ diagram that is populated by the intermediate-mass binary pulsars (Fig. 2). The orbital period is 3.016 days and the companion has a minimum mass of 0.87 $M_\odot$. The minimum mass of the companion is sufficeintly high that measurement of Shapiro delay is possibly if the system has a low inclination angle. However, due to the large uncertainty in the proper motion and the large effect of DM variation on the TOAs at LOFAR frequencies, we are unable to measure any Shapiro delay.

We also found that the pulsar shows temporal variation in DM across the observing span. We modelled the DM variation by measuring the average DM value over spans of 30

Table 8. Timing Solution of PSR J1658+3630, obtained by fitting the TOAs with the rotational, positional and orbital parameters of the pulsar. The proper motion of the pulsar is fixed at the estimated value obtained through archival optical imaging data.

Timing Parameter	Value
Right Ascension, RA (J2000)	16:58:26.5198(3)
Declination, Dec (J2000)	+36:30:30.095(3)
Spin frequency, ν (s^{-1})	30.277356639727(13)
Spin frequency Derivative, $\dot{\nu}$ (10^{-16} s^{-2})	-1.061(17)
DM[a] (pc cm^{-3})	3.04387(3)
Proper motion, RA (arcsec yr^{-1})	0.015(8)
Proper motion, Dec (arcsec yr^{-1})	−0.065(8)
Epoch of timing solution (MJD)	58073
Epoch of position (MJD)	58073
Solar system ephemeris model	DE405
Clock correction procedure	TT(TAI)
Time units	TCB
Timing Span (MJD)	57777-58439
Number of TOAs	399
Weighted post-fit residual (μs)	20.6
Reduced χ^2 value	5.3
Binary Parameter	
Orbital period, P_b (days)	3.0163073825(13)
Projected Semi-major Axis, $a_p \sin i$ (lt-s)	10.4497253(14)
Epoch of Ascending Node, T_{asc} (MJD)	57768.17408579(15)
First Laplace-Lagrange parameter, ϵ_1 (10^{-5})	2.14(3)
Second Laplace-Lagrange parameter, ϵ_2 (10^{-5})	−2.17(3)
Binary Model	ELL1
Derived Parameter	
Spin Period, P (s)	0.033027982326829(13)
Spin Period Derivative, $\dot{P}$ (10^{-20} s s^{-1})	11.57(19)
Orbital Eccentricity, e (10^{-5})	3.05(3)
Longitude of Periastron, ω (°)	135.3(5)
Epoch of Periastron, T_0 (MJD)	57769.308(4)
DM distance/NE2001 (kpc)	0.49
DM distance/YMW16 (kpc)	0.22
Characteristic Age (Gyr)	4.5
Surface Magnetic Field Strength (10^9 G)	2.0
Mass Function ($M_\odot$)	0.13466234(2)
Minimum Companion Mass ($M_\odot$)	0.8731
Spin-down luminosity (10^{30} erg s^{-1})	127

[a] This is the reference DM to measure the temporal DM variation of the pulsar.

days. The measured DM value in each epoch is then compared to the average across the observing span and is shown in Fig. 9. We found that for most of the time, the DM value fluctuates between −0.0002–+0.0001 pc cm^{-1} around the average DM value of 3.04387 pc cm^{-1}, with the exception of two epochs where the DM is measured to be approximately 0.00025 and 0.0005 pc cm^{-1} more than the average, respectively. The timing solution took into consideration the measured DM variation.

The binary parameters and the nearness (0.22–0.49 kpc) suggest that the companion might be visible in archival optical imaging data. At the position of the pulsar, we found an r = 22.2 magnitude optical counterpart, in both the Sloan Digital Sky Survey (SDSS, York et al. 2000; Albareti et al. 2017) and the Panoramic Survey Telescope and Rapid Response System (Pan-STARRS, Chambers et al. 2016; Flewelling et al. 2016) images. The optical properties of the companion agree with the orbital properties from the interim timing solution, that it is most likely a Carbon-Oxygen white dwarf. Later, we found that the position of the pulsar obtained from the timing solution is offset from both the SDSS observation taken in 2000 and the Pan-STARRS observation taken in 2014. From the offsets, we measured a proper motion of $+0\farcs015 \pm 0\farcs008$ yr^{-1} in right ascension and $-0\farcs065 \pm 0\farcs008$ yr^{-1} in declination. The proper motion estimated here is large enough that a sinusoidal variation with increasing amplitude will be seen in the timing data if it is not accounted for. As we only have one and a half years of timing data, we were not able to refine the measured proper motion through pulsar timing yet. Hence, we fixed the proper motion of the pulsar at the values measured while refining the other properties.

While the timing model is able to broadly describe the rotational and orbital properties of the pulsar, we note that there remains a significant timing residual in the TOAs and a poor χ^2_{red} value. There are several possible contributions

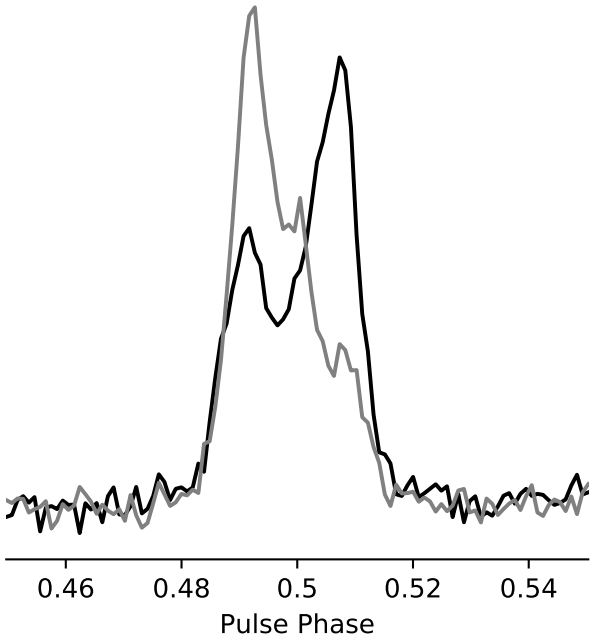

Figure 7. The integrated pulse profiles of the two different modes of PSR J1657+3304, overlaid on top of each other. The more commonly occurring double-peaked mode is in black and the less common single-peaked mode is in grey.

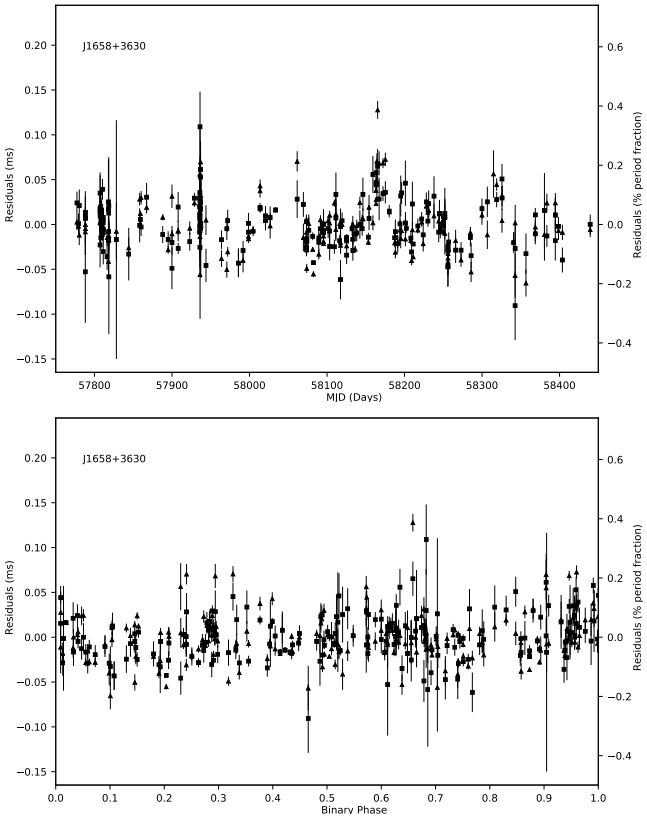

Figure 8. The residuals of the timing model of PSR J1658+3630. The different symbols represents the different observing frequencies, with the triangles representing the lower part of the LOFAR and GLOW bands (central frequencies of 128 MHz and 140 MHz, respectively) and squares for the upper part of the LOFAR and GLOW bands (central frequencies of 167 MHz and 171 MHz, respectively).

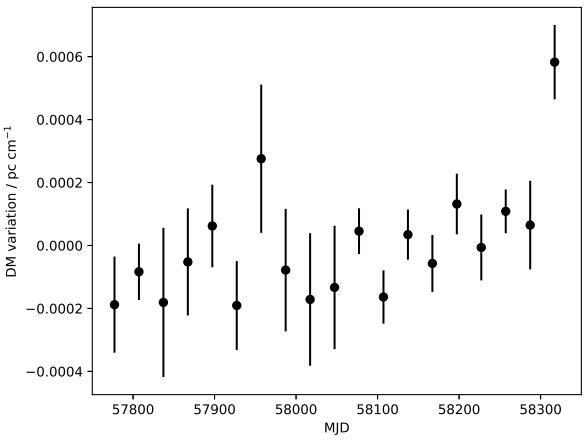

Figure 9. The modelled DM variation of PSR J1658+3630 over the observing span.

to the large timing residuals. First, the proper motion measured has a significant uncertainty of $0\farcs008$ yr^{-1} in both right ascension and declination. The proper motion can be measured to a higher precision with pulsar timing, but this will require a longer observing span on the order of several years. We also noticed that there is an unmodelled extra delay on the timing residuals at around MJD 58165. This is likely a short duration increase in the DM of the pulsar on a time-scale shorter than the 30 days used to model the DM variation of the pulsar.

The average pulse profile integrated over the observing span shows frequency dependant profile evolution. Figure 10 shows the integrated pulse profiles at 4 different LOFAR sub-bands and at 334 MHz, overlaid with the model that best describes the pulse profiles. The profiles in the LOFAR bandwidth are described by 3 Von Mises components, corresponding to the leading bump, the main peak and a small trailing component that increases in relative intensity to the main peak as the observing frequency increases. The profile at 334 MHz has a much lower S/N and was fitted with just 2 components. We are unable to identify if the trailing component is present at 334 MHz. We also measured the width of the pulses at 50% and 10% of the maximum, shown in Table 9.

The pulsar is also observed to undergo diffractive scintillation in some of the observations. While the study of the scintillation properties of the pulsar will be presented in a separate paper, we note that the presence of diffractive scintillation might affect the overall pulse profile shape of individual observations due to the variation in flux densities in different parts of the bandwidth at different observing

Table 9. The flux densities and pulse widths of the PSR J1658+3630 at 4 different LOFAR sub-bands of 118.8, 140.3, 158.6 and 178.0 MHz and at 334 MHz measured with the detection with the Lovell telescope. The upper limit of the flux density of PSR J1658+3630 based on the non-detection at 1532 MHz is also quoted, estimated using the average W_{50} value of the detection made at 334 MHz and a 1-hour integration time.

Frequency MHz	Flux density mJy	W_{10} ms	δ_{50} %	W_{50} ms	δ_{50} %
118.8	24(8)	6.282(16)	19.03(5)	0.6977(10)	2.113(3)
140.3	17(6)	6.12(2)	18.54(6)	0.6768(11)	2.050(3)
158.6	10(4)	6.41(2)	19.40(6)	0.6712(15)	2.033(5)
178.0	6(2)	6.89(5)	20.88(15)	0.744(3)	2.252(9)
334.0	1.7(3)	7.42(19)	22.4(6)	1.5(2)	4.4(7)
1532.0	<0.06	–	–	–	–

epochs and subsequently affecting the timing precision of these observations due to profile shape changes relative to the template used. The DM variation can affect the overall shape of the profile as well, as different parts of the bandwidth are not aligned at the fiducial point of the template.

We also calculated the average flux densities of PSR J1658+3630 at the same 4 LOFAR sub-bands and the flux density from the 334 MHz observation in which the pulsar is detected. The average flux densities at LOFAR frequencies were calculated from of 41 observations (Table 9). The diffractive scintillation and possibly refractive scintillation will result in variation in the flux densities. We model the spectral index of the pulsar using a single power law, shown in Figure 11, and measured $\alpha = -2.5 \pm 0.7$. The pulsar is therefore a steep spectrum source, similar to the other MSPs discovered by LOFAR (Bassa et al. 2017; Pleunis et al. 2017). The spectral index predicts a radio luminosity at 1400 MHz, L_{1400} of between 0.0015 and 0.007 mJy kpc^2, depending on the distance obtained by the electron density model used (Cordes & Lazio 2002; Yao et al. 2017). This is similar to another recently discovered nearby, low-luminosity MSP J2322−2650 ($L_{1400} = 0.008$ mJy kpc^{-2}; Spiewak et al. 2018), strengthening the argument that there could be a large population of low-luminosity Galactic MSPs that can only be detected at very low radio frequencies.

7 CONCLUSIONS

We have presented the properties of 21 pulsars discovered by the LOFAR Tied-Array All-Sky Survey (LOTAAS). We have obtained the rotational properties of the pulsars, which suggest that most of the pulsars discovered are of an older population of $\tau_c \geq 10$ Myr. We have also studied the frequency evolution of the integrated pulse profiles of the pulsars, where we found that several pulsars showed frequency evolution that is contrary to the Radius-Frequency-Mapping model. Besides that, we have measured the spectral indices of the pulsars and found that the average spectral index of the sample to be lower than the known pulsar population, possibly linking the spectral properties with the age of the pulsars. However, a larger sample of pulsars is required to confirm this relationship. Finally, we modelled the various properties of the first binary pulsar discovered by LOTAAS, showing that the pulsar is in a binary system with a Carbon-Oxygen white dwarf with a minimum mass of $0.87 M_\odot$. The pulsar is also found to be an ultra steep spectrum source, giving an estimated radio luminosity at 1400 MHz between 0.0015 and 0.007 mJy kpc^2, suggesting that it is part of a possible nearby, low-luminosity millisecond pulsars.

ACKNOWLEDGEMENTS

REFERENCES

Albareti F. D., et al., 2017, ApJS, 233, 25
Alpar M. A., Cheng A. F., Ruderman M. A., Shaham J., 1982, Nature, 300, 728
Bassa C. G., et al., 2017, ApJ, 846, L20
Bates S. D., Lorimer D. R., Verbiest J. P. W., 2013, MNRAS, 431, 1352
Bhattacharya D., van den Heuvel E. P. J., 1991, Phys. Rep., 203, 1
Bilous A. V., et al., 2016, A&A, 591, A134
Chambers K. C., et al., 2016, preprint, (arXiv:1612.05560)
Chen K., Ruderman M., 1993, ApJ, 402, 264
Coenen T., et al., 2014, A&A, 570, A60
Cordes J. M., 1978, ApJ, 222, 1006
Cordes J. M., Lazio T. J. W., 2002, preprint, (arXiv:0207156)
Edwards R. T., Hobbs G. B., Manchester R. N., 2006, MNRAS, 372, 1549
Flewelling H. A., et al., 2016, arXiv e-prints, p. arXiv:1612.05243
Geyer M., Karastergiou A., 2016, MNRAS, 462, 2587
Geyer M., et al., 2017, MNRAS, 470, 2659
Haslam C. G. T., Salter C. J., Stoffel H., Wilson W. E., 1982, A&AS, 47, 1
Hassall T. E., et al., 2012, A&A, 543, A66
Hobbs G. B., Edwards R. T., Manchester R. N., 2006, MNRAS, 369, 655
Hotan A. W., van Straten W., Manchester R. N., 2004, Publ. Astron. Soc. Australia, 21, 302
Jankowski F., van Straten W., Keane E. F., Bailes M., Barr E. D., Johnston S., Kerr M., 2018, MNRAS, 473, 4436
Kijak J., Lewandowski W., Maron O., Gupta Y., Jessner A., 2011, A&A, 531, A16
Kondratiev V. I., et al., 2016, A&A, 585, A128
Kramer M., Lyne A. G., O'Brien J. T., Jordan C. A., Lorimer D. R., 2006, Science, 312, 549
Lange C., Camilo F., Wex N., Kramer M., Backer D. C., Lyne A. G., Doroshenko O., 2001, MNRAS, 326, 274
Lawson K. D., Mayer C. J., Osborne J. L., Parkinson M. L., 1987, MNRAS, 225, 307
Lorimer D. R., Kramer M., 2005, Handbook of Pulsar Astronomy
Lyne A., Hobbs G., Kramer M., Stairs I., Stappers B., 2010, Science, 329, 408
Perera B. B. P., Stappers B. W., Weltevrede P., Lyne A. G., Bassa C. G., 2015, MNRAS, 446, 1380

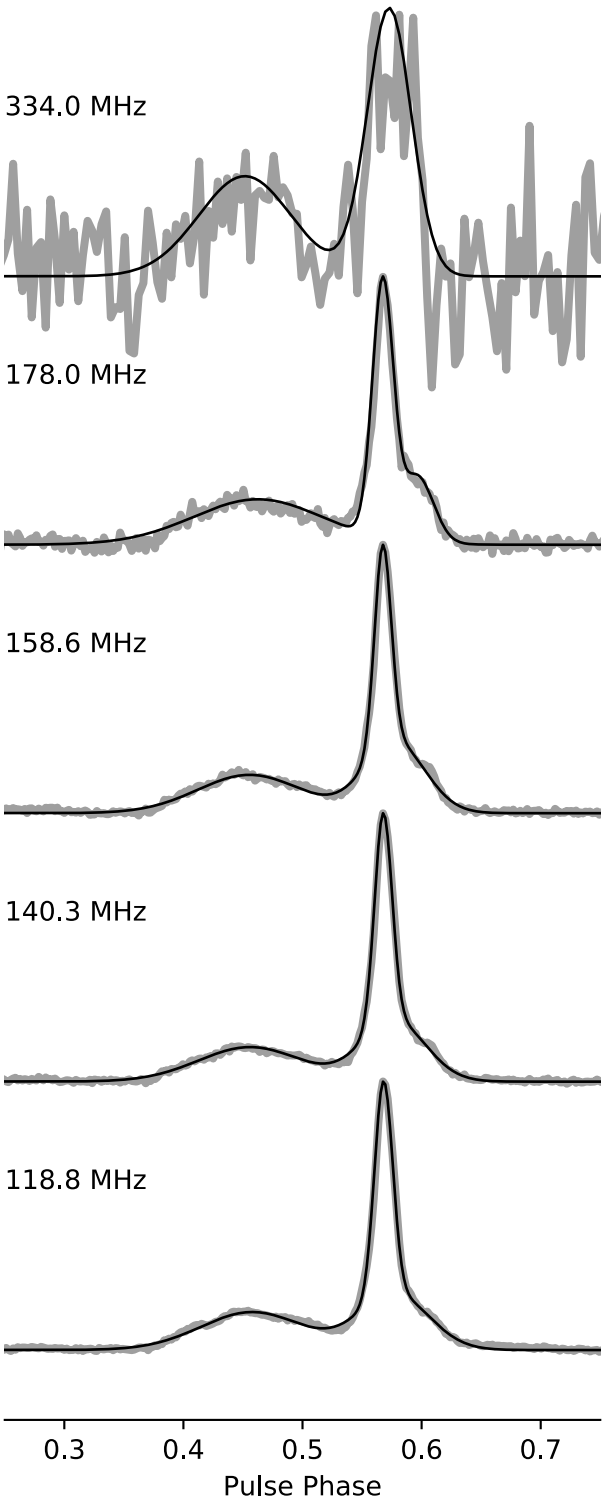

Figure 10. The integrated pulse profiles of PSR J1658+3630 at several different sub-bands obtained with the LOFAR core and at 334 MHz obtained with the Lovell Telescope. The profiles are overlaid with the models that describe the profiles at different observing frequencies in order to study profile evolution.

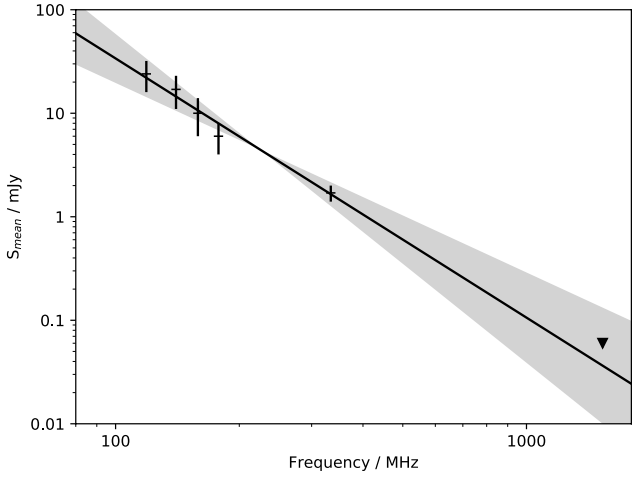

Figure 11. The spectrum of PSR J1658+3630, modelled with a single power law. The triangle is the upper limit in flux density at 1532 MHz estimated from a 1-hour non-detection with the Lovell telescope. The black line is the best-fit spectral index of −2.5 and the grey shaded region is the 1σ uncertainty in the fitted spectral index.

Pilia M., et al., 2016, A&A, 586, A92
Pleunis Z., et al., 2017, ApJ, 700, 1
Rajwade K., Lorimer D. R., Anderson L. D., 2016, MNRAS, 455, 493
Reich P., Reich W., 1988, A&A, 196, 211
Ruderman M. A., Sutherland P. G., 1975, ApJ, 196, 51
Sanidas S., et al., 2019, arXiv e-prints, p. arXiv:1905.04977
Spiewak R., et al., 2018, MNRAS, 475, 469
Stappers B. W., et al., 2011, A&A, 530, A80
Tyul'bashev S. A., Tyul'bashev V. S., Oreshko V. V., Logvinenko S. V., 2016, Astronomy Reports, 60, 220
Tyul'bashev S. A., et al., 2017, Astronomy Reports, 61, 848
Tyul'bashev S. A., Tyul'bashev V. S., Malofeev V. M., 2018, A&A, 618, A70
Wang N., Manchester R. N., Johnston S., 2007, MNRAS, 377, 1383
Yao J. M., Manchester R. N., Wang N., 2017, ApJ, 835, 29
York D. G., et al., 2000, AJ, 120, 1579
van Haarlem M. P., et al., 2013, A&A, 556, A2
van Straten W., Bailes M., 2011, Publ. Astron. Soc. Australia, 28, 1

This paper has been typeset from a TEX/LATEX file prepared by the author.